BNL-225714-2024-JAAM

GRP-COCA-31

Theoretical Prediction and Experimental Verification of IrOx Supported on Titanium Nitride for Acidic Oxygen Evolution Reaction

X. Han, J. G. Chen

To be published in "Journal of the American Chemical Society"

June 2024

Chemistry Department

Brookhaven National Laboratory

U.S. Department of Energy

USDOE Office of Science (SC), Basic Energy Sciences (BES)

DISCLAIMER

Theoretical Prediction and Experimental Verification of IrO_x Supported on Titanium Nitride for Acidic Oxygen Evolution Reaction

Xue Han, ‡, [a] Tianyou Mou, ‡, [a] Arephin Islam, [a] Sinwoo Kang, [a, c] Qiaowan Chang, [a, b] Zhenhua Xie, [a, c] Xueru Zhao, [a] Kotaro Sasaki, [a] José A. Rodriguez, [a] Ping Liu, *, [a] Jingguang G. Chen *, [a, c]

[a] Chemistry Division, Brookhaven National Laboratory, Upton, New York 11973, United States

[b] School of Chemical Engineering and Bioengineering, Washington State University, Pullman, Washington 99164, United States

[c] Department of Chemical Engineering, Columbia University, New York, New York 10027, United States

ABSTRACT: Reducing iridium (Ir) catalyst loading for acidic oxygen evolution reaction (OER) is a critical strategy for large-scale hydrogen production via proton exchange membrane (PEM) water electrolysis. However, simultaneously achieving high activity, long-term stability, and reduced material cost remains challenging. To address this challenge, we develop a framework by combining density functional theory (DFT) prediction using model surfaces and proof-of-concept experimental verification using thin films and nanoparticles. DFT results predict that oxidized Ir monolayers over titanium nitride (IrO_x/TiN) should display higher OER activity than IrO_x while reducing Ir loading. This prediction is verified by depositing Ir monolayers over TiN thin films via physical vapor deposition. The promising thin film results are then extended to commercially viable powder IrO_x/TiN catalysts, which demonstrate a lower overpotential and higher mass activity than commercial IrO_2, and a long-term stability of 250 hours to maintain a current density of 10 mA cm^{-2}. The superior OER performance of IrO_x/TiN is further confirmed using proton exchange membrane water electrolyzer (PEMWE), which shows a lower cell voltage than commercial IrO_2 to achieve a current density of 1 A cm^{-2}. Both DFT and *in situ* X-ray absorption spectroscopy reveal that the high OER performance of IrO_x/TiN strongly depends on the IrO_x-TiN interaction via direct Ir-Ti bonding. This study highlights the importance of close interaction between theoretical prediction based on mechanistic understanding and experimental verification based on thin film model catalysts to facilitate the development of more practical powder IrO_x/TiN catalysts with high activity and stability for acidic OER.

1. INTRODUCTION

Activity, stability, and material cost are three critical factors when designing acid oxygen evolution reaction (OER) electrocatalysts for practical applications. [1-5] To date, iridium oxide (IrO_x)-based materials are the best acidic OER electrocatalysts that can meet the stability requirement under harsh operating conditions. [6-8] However, high costs and scarcity of Ir limit large-scale applications of IrO_x. [7, 9-11] Therefore, it is imperative to discover OER electrocatalysts with reduced Ir loading while maintaining their catalytic activity and stability in the acid environment.

Depositing Ir-based materials on a support is a promising method to reduce the overall Ir loading and tune the Ir-support interactions to enhance the OER performance[12, 13]. Transition metal nitrides have been recently identified as promising support materials for electrocatalysts due to their high electrical conductivity and low costs. [14-18] Particularly, titanium nitride (TiN) holds the merits of metal-like conductivity[19, 20] and excellent resistance to acidic oxidation[15], making it a promising support for Ir. Several studies have been reported for Ir oxides deposit on TiN in the form of IrO_2@Ir/TiN (60 wt. % of Ir on TiN) [21], IrO_2@Ir/TiN (40 wt. % of Ir on TiN) [22] and IrO_2/TiN[23]. However, these reported electrocatalysts contained a high content of Ir, and their electrocatalytic stability was rather low (<10 hours at 10 mA cm^{-2}). Meanwhile, a comprehensive understanding, coupled with theoretical calculations and *in situ* characterization, of the structure-activity-stability correlation to advance the OER performance of TiN-supported Ir and IrO_x, remains unclear.

Herein, we develop a framework for designing active and stable materials for acidic OER based on density functional theory (DFT) predictions and proof-of-concept experimental verification of thin films and nanoparticles. A partially oxidized Ir (IrO_x) overlayer on a TiN support was selected for DFT calculations to reduce the Ir loading to a few monolayers while maintaining a similar number of active sites. In addition, such a model system also allows direct verification by experimental studies, as recently demonstrated for nitride-supported Pt for the hydrogen evolution reaction. [24] Using the binding energy of *OH (* denotes adsorbed intermediates) as the OER reactivity descriptor for IrO_x/TiN, the OER activity was found to be improved by increasing the Ir coverage from one to three monolayers (MLs), and the trend was confirmed by the experimentally synthesized IrO_x/TiN film model catalysts. For practical

applications, the promising thin film results were extended to powder-based catalysts with IrO_x deposited on TiN nanoparticles (IrO_x/TiN NPs). The IrO_x/TiN NPs exhibited excellent acidic OER performance, requiring a minimum overpotential of 293 mV at 10 mA cm^{-2} and long-term stability of 250 hours with neglect degradation. The mass activity of IrO_x/TiN with a reduced Ir loading of 40 μg_{Ir} cm^{-2} achieved 270.8 A g_{Ir}^{-1}, significantly higher than the benchmark commercial IrO_2 (C-IrO_2). When further integrated into a proton exchange membrane water electrolyzer (PEMWE) cell with the IrO_x/TiN catalyst at a low Ir loading of 0.2 mg cm^{-2}, only 1.69 V was required to achieve a current density of 1 A cm^{-2}, lower than that using C-IrO_2 (above 1.8 V). *In situ* X-ray absorption spectroscopy (XAS) characterization further revealed the transition of Ir to IrO_x under OER conditions, as well as the presence of the Ir-Ti bond to highlight the interaction between IrO_x and TiN. According to the DFT results, the direct Ir-Ti bonding tuned the binding strength of *OH on the IrO_x layer, leading to a higher OER activity than bulk IrO_2 while still maintaining high stability under the acidic OER condition. Overall, DFT calculations of the overlayer models predict an overpotential trend of 1ML > 2ML > 3ML IrO_x over the TiN substrate, which is then verified by experiments over TiN thin films with the corresponding coverages of IrO_x. These findings provide guidance to prepare the nanoparticle catalysts for more practical and commercial applications, and IrO_x/TiN NPs show a better catalytic performance toward acidic OER than C-IrO_2. More importantly, this study highlights the importance of integrating theoretical prediction and experimental studies of well-characterized thin film catalysts to facilitate the development of commercially viable powder-based nanoparticle OER catalysts with enhanced activity and promising stability.

2. RESULTS AND DISCUSSION

2.1 DFT prediction of structure-activity relationships of OER over TiN-supported Ir-based catalysts

The TiN-supported IrO_x overlayers are potential candidates for OER acidic catalysts, which require a design principle of reducing the loading of Ir while maintaining a similar OER activity. The TiN(100) surface was chosen since it was known to be the most stable termination of TiN.[25] 1ML, 2ML, and 3ML of Ir that adopted face-centered-cubic (111) arrangement were placed on TiN(100) to capture the high-coordinated sites at the terrace of supported IrO_x NPs. Under acidic OER reaction conditions (> 1.5 V vs. RHE), the surface oxidation, as observed previously,[26-28] was described by the chemisorption of oxygen or *O on the surface and subsurface of Ir overlayers. The surfaces covered by *OH or *OH/*O mixture were not considered due to the favorable deprotonation of *OH to *O with more negative values in the reaction free energy (ΔG) under the reaction potentials (**Figure S1** and **Table S2**). Specifically, three model systems were constructed, including 1ML Ir with *O covered on the surface (1ML-IrO_x/TiN overlayer, **Figure 1a**), 2ML Ir (2ML-IrO_x/TiN overlayer, **Figure 1b**), and 3ML of Ir (3ML-IrO_x/TiN overlayer, **Figure 1c**) with *O covered on the surface and occupied at the subsurface underneath. For comparison, Ir(111) with *O covered on either the surface (1ML-IrO_x, **Figure 1d**) or both surface and subsurface (2ML-IrO_x, **Figure 1e**), were also considered to identify the effect of the TiN support. An oxygen-covered IrO_x nanoparticle was constructed to represent the perimeter sites of IrO_x NPs, where both the low-coordinated IrO_x sites and TiN were exposed to the reactants and participated in the reaction directly (IrO_x/TiN interface, **Figure 1f**). An IrO_2(110) surface (IrO_2, **Figure S2**) was also included as a reference.

The two widely used OER mechanisms, the adsorbate evolution mechanism (AEM) and the lattice oxygen-participating mechanism (LOM), were considered in this work (**Figure S3**).[27, 29] However, for the IrO_x/TiN catalysts, only surface-adsorbed oxygen is involved in the reaction. Thus, LOM is changed to the surface oxygen mechanism (SOM). As demonstrated below, different from LOM, the structure of

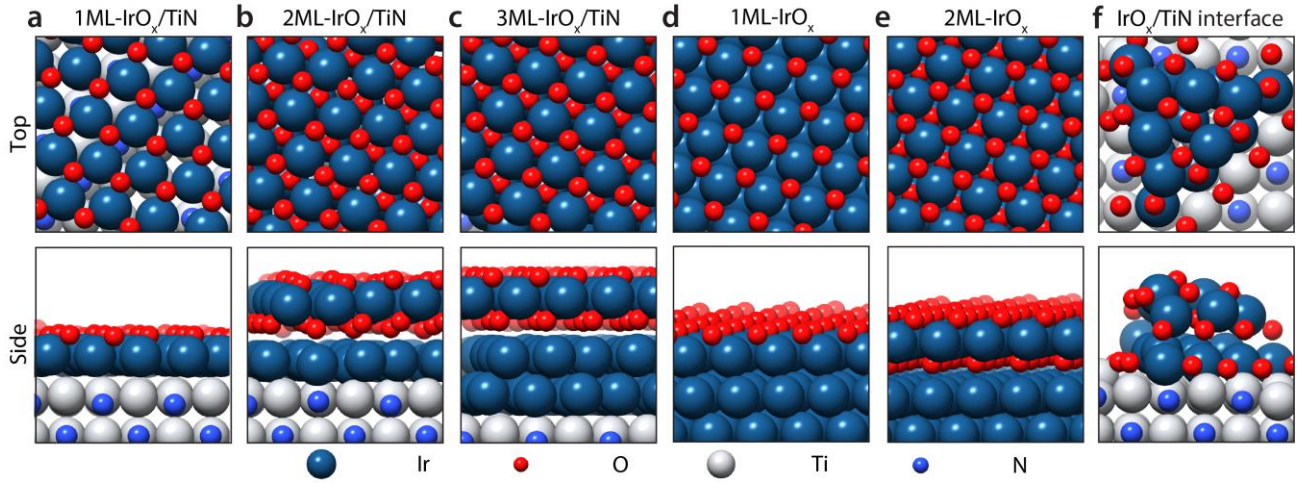

Figure 1. Top (top) and side (bottom) view of a) 1ML-IrO_x/TiN, b) 2ML-IrO_x/TiN, c) 3ML-IrO_x/TiN, d) 1ML-IrO_x, e) 2ML-IrO_x, and f) IrO_x/TiN interface models optimized using DFT.

IrO_x is barely affected by the removal of surface oxygen, and the resulting vacancies are easily filled to ensure stability during OER operation. The SOM mechanism starts with an oxygen vacancy (O-v) adjacent to an *O on the surface, at which H_2O from the electrolyte adsorbs in the form of $*H_2O$, which undergoes a spontaneous dissociation to *OH at the water-IrO_x/TiN interface, along with a proton transfer to the solvation and form H_3O^+ (**Figure S4**). The O-O coupling of produced *OH and neighboring *O forms $*O_2$ (**Figure S5b**), which is unstable on the surface and prefers desorption to O_2 at room temperature (ΔG = -0.20 eV). Due to the low stability, neither $*H_2O$ nor $*O_2$ is involved in the OER on IrO_x/TiN. The cycle is closed by additional H_2O dissociative adsorption and deprotonation to form *O and regenerate an O-v site (see **supporting information** (**SI**) for more details of the reaction mechanism).

According to the DFT-calculated potential free energy diagram at zero potential (0 V vs. RHE) in **Figure 2**, the potential limiting step (PDS) that corresponds to the maximum free energy change (ΔG_{max}) among the elementary steps is the O-O coupling of *OH and *O for 1ML-IrO_x/TiN and 2ML-IrO_x/TiN overlayers and the IrO_x/TiN interface, while the magnitude is different. The DFT-predicted ΔG_{max} and thus the theoretical OER overpotentials (η) for the overlayer surfaces (ΔG_{max} = 2.01 eV and η = 0.78 V for 1ML-IrO_x/TiN; ΔG_{max} = 1.73 eV and η = 0.50 V for 2ML-IrO_x/TiN, **Figures 2a** and **b**) are much lower than that of the IrO_x/TiN interface (ΔG_{max} = 4.79 eV and η = 3.56 V, **Figure S6**). The PDS for 3ML-IrO_x/TiN and IrO_x is changed to the activation of H_2O to form *OH. The 3ML-IrO_x/TiN overlayer shows a lower η (ΔG_{max} = 1.71 eV and η = 0.48 V, **Figure 2c**) than the IrO_x surfaces (ΔG_{max} = 2.02 eV and η = 0.79 V for 1ML-IrO_x; ΔG_{max} = 2.35 eV and η = 1.12 V for 2ML-IrO_x, **Figures 2d** and **e**). For both IrO_x/TiN and IrO_x systems investigated in the current study, the OER via AEM is less competitive than that via SOM due to the low stability of the *OOH intermediate (see **SI**, **Figures S5a** and **S7** for details) [27].

The DFT-predicted OER overpotential strongly depends on the *OH binding energy (ΔG_{*OH}) of the IrO_x-based systems via a volcano-like relationship (**Figure 2f**), while the binding of *O (ΔG_{*O}) [30] and the binding difference between *O and *OH (ΔG_{*O}-ΔG_{*OH}) [31], which were proposed previously as descriptors for AEM on diverse types of metal oxides[31], do not work well in the current study due to a difference in the preferred reaction pathway. Comparing the IrO_x/TiN interface with the IrO_x overlayers, a significant decrease in ΔG_{*OH} is observed, where the direct IrO_x-TiN interaction stabilizes *OH compared to IrO_x (**Figure 2f**). To maximize the OER activity, the binding of *OH at the Ir site should be moderate. Specifically, along the left side of the volcano, weakening of *OH binding at IrO_x-TiN is desirable to facilitate the PDS, O-

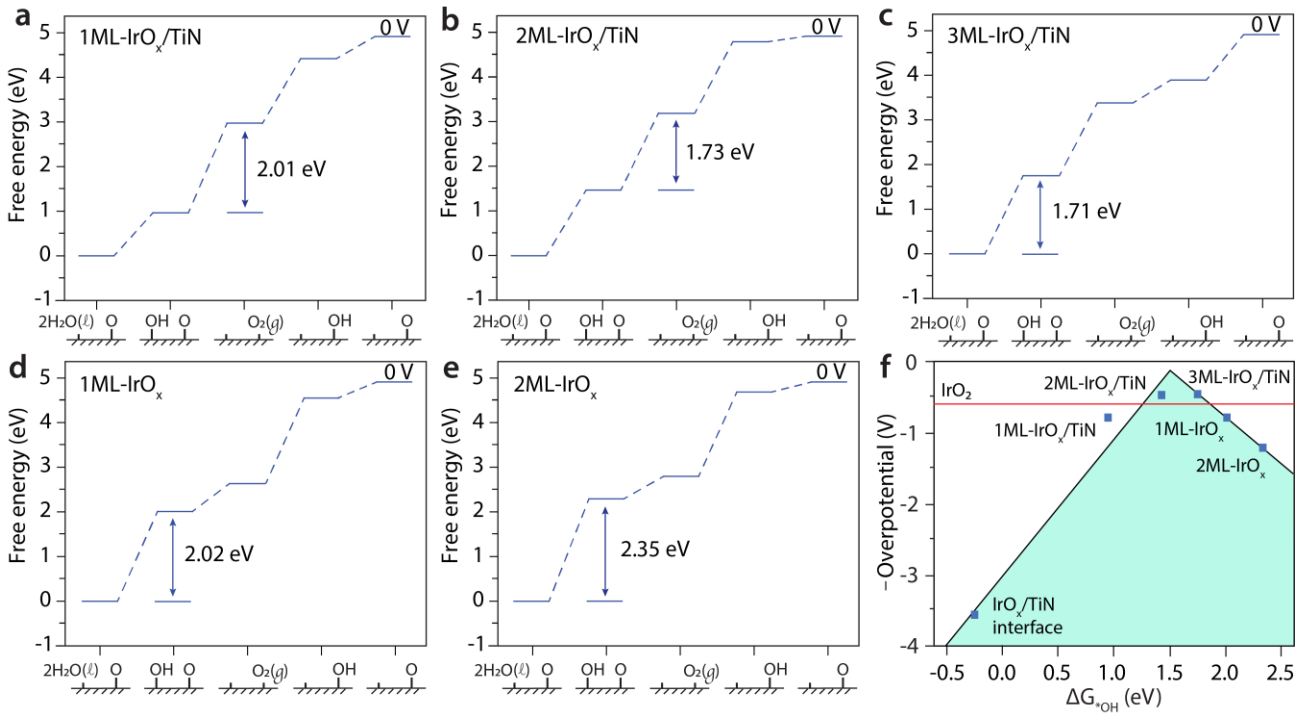

Figure 2. DFT-calculated free energy diagrams for acidic OER on a) 1ML-IrO_x/TiN, b) 2ML-IrO_x/TiN, c) 3ML-IrO_x/TiN, d) 1ML-IrO_x, and e) 2ML-IrO_x. f) Volcano plot of the negative value of overpotential (-η) versus the Gibbs free adsorption energy of *OH (ΔG_{*OH}). Six systems were included, while IrO_2 was plotted as a red line for reference.

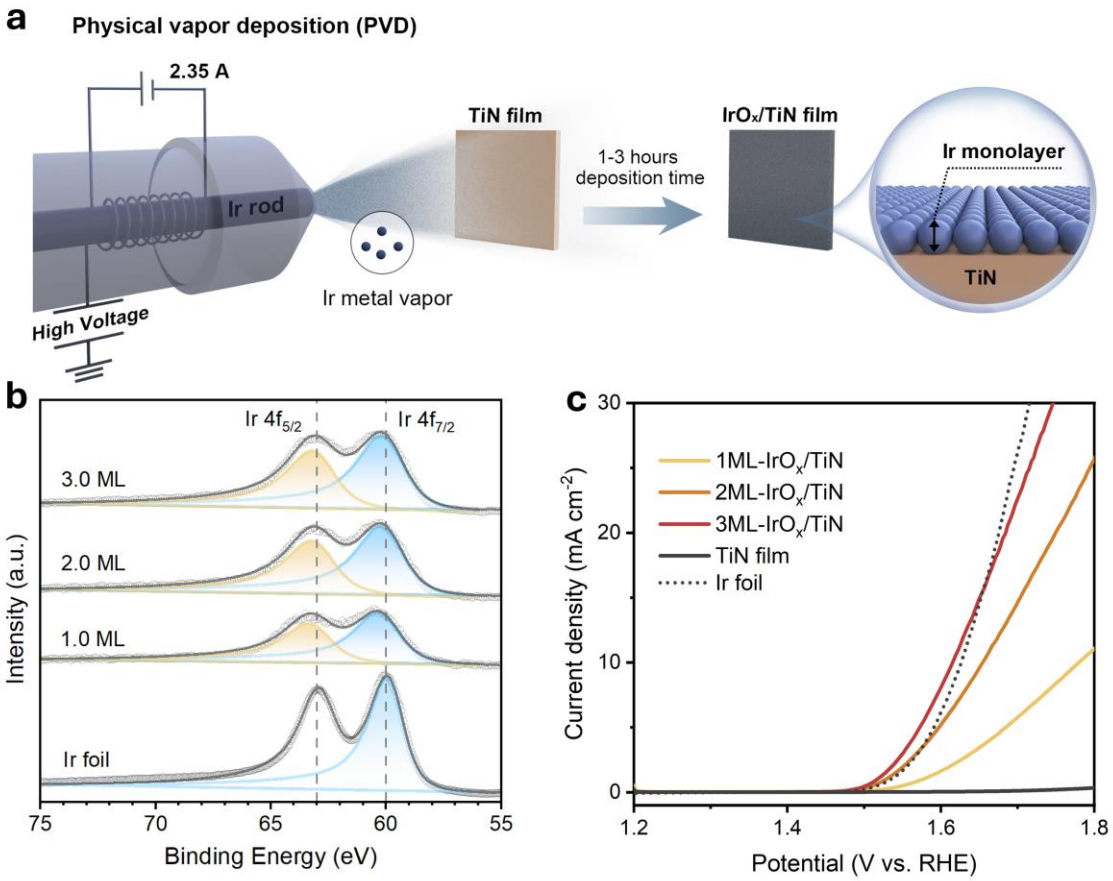

Figure 3. a) Schematic illustration of the procedure used for synthesizing IrO_x/TiN films by using the physical vapor deposition method. b) Ir 4f XPS spectra of 1ML-, 2ML-, and 3ML-IrO_x/TiN films, and Ir foil. c) LSV curves of 1ML-, 2ML-, and 3ML-IrO_x/TiN films, an Ir foil, and a plain TiN film.

OH coupling, and thus the overall OER, which is well demonstrated by the decreased OER overpotential via the sequence of 2ML-IrO_x/TiN overlayer < 1ML-IrO_x/TiN overlayer < IrO_x/TiN interface. While along the right side of the volcano, a stronger binding of *OH favors the corresponding PDS, H_2O dissociation to *OH. The *OH binding is overly weakened for IrO_x due to the lack of interaction with the TiN support, while in the presence of the TiN support, the *OH binding is strengthened on the 3ML-IrO_x/TiN overlayer. Correspondingly, the OER overpotential follows the sequence of 3ML-IrO_x/TiN overlayer < 1ML-IrO_x < 2ML-IrO_x.

According to the DFT results, to achieve a high OER activity, the IrO_x-TiN interaction is essential, where all IrO_x/TiN systems bind *OH more strongly and display lower η than IrO_x alone (**Figure 2f**). In addition, the amount of Ir matters. An increase in coverage of Ir from 1ML to 3ML weakens the binding of *OH, leading to a change in the PDS from O-OH coupling for 1ML-IrO_x/TiN and 2ML-IrO_x/TiN overlayers to H_2O dissociation for the 3ML-IrO_x/TiN overlayer. Among all overlayer models, both 2ML-IrO_x/TiN and 3ML-IrO_x/TiN overlayers exhibit lower η than IrO_2, where 3ML-IrO_x/TiN is the most active system due to the near optimum *OH binding energy (**Figure 2f**). Therefore, thin overlayers of IrO_x on TiN represent the possibility of reducing the loading of Ir while maintaining similar performance, especially for 3ML-IrO_x/TiN, which shows a comparable or slightly higher activity than IrO_2 (**Figure S8**).

2.2 Synthesis and acidic OER performance of Ir monolayers deposited on TiN films

Guided by the DFT prediction, thin film IrO_x/TiN catalysts were synthesized using physical vapor deposition (PVD) within an ultra-high vacuum (UHV) chamber (**Figure 3a**). Various Ir coverages with 1ML, 2ML, and 3ML on TiN films were synthesized, denoted as 1ML-, 2ML-, and 3ML-IrO_x/TiN films. The X-ray photoelectron spectroscopy (XPS) results of the Ir 4f region of these as-prepared films (**Figure 3b**) show that the peak features of Ir $4f_{7/2}$ and Ir $4f_{5/2}$ are primarily attributed to metallic Ir. These peaks slightly shift to a higher binding energy than the Ir foil, likely due to the

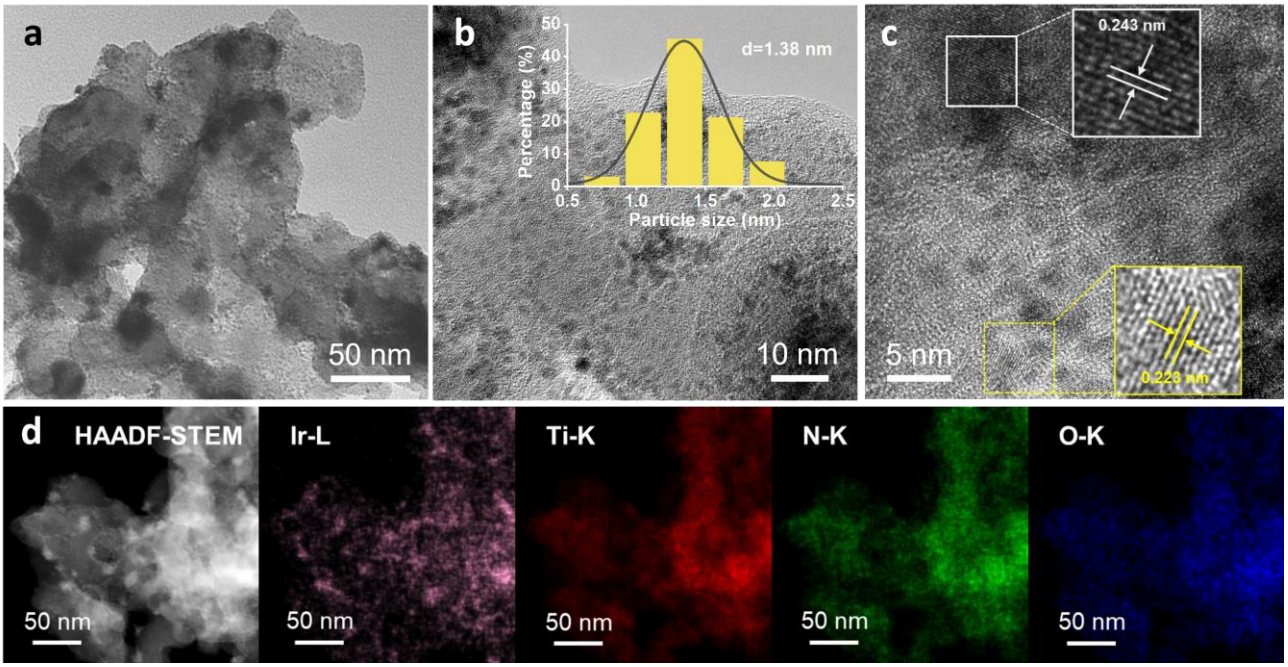

Figure 4. Structural characterization of IrO_x/TiN NPs. a-c) TEM images with different magnifications; the insert in b) is corresponding particle size distribution of IrO_x; d) HAADF-STEM images and the corresponding X-EDS mappings.

surface oxidation of Ir and possible interaction between Ir and the TiN support. The Ti 2p spectra of IrO_x/TiN films (**Figure S11**) can be deconvoluted into two sets of peaks, corresponding to TiN and TiON, respectively.

The acidic OER performance of 1ML-, 2ML-, and 3ML-IrO_x/TiN films, as well as an Ir foil and a TiN film as standards, was evaluated using linear sweep voltammetry (LSV) in O_2-saturated 0.1 M $HClO_4$ in a three-electrode cell. **Figure 3c** shows that the 3ML-IrO_x/TiN film demonstrates the best OER activity with an overpotential of 385 mV at 10 mA cm^{-2}, outperforming the Ir foil standard (396 mV), 2ML-IrO_x/TiN film (423 mV), and 1ML-IrO_x/TiN film (550 mV). The overall activity trend of the IrO_x/TiN films is consistent with the DFT prediction in **Figure 2f**. Additionally, a more oxidized Ir with 3ML on TiN thin film (3ML-IrO_x/TiN-H) was synthesized using the PVD method and characterized using XPS, and the electrochemical results showed that it had lower OER activity than the 3ML-IrO_x/TiN film and the Ir foil (**Figure S12**).

The stability test of IrO_x/TiN films (**Figure S13**) shows severe degradation within 1 hour, likely due to the weak interaction between Ir and TiN synthesized by the PVD method. As discussed next, the interaction between IrO_x and TiN is significantly improved in powder IrO_x/TiN catalysts.

2.3 Synthesis and characterization of IrO_x/TiN nanoparticles

The synthesis strategy of powder-based nanoparticle catalysts aims to deposit Ir on TiN NPs, fostering a strong metal-support interaction and, therefore, enhancing the acidic OER performance. The synthesis of TiN NPs was modified according to a reported method[32] (**Figure S14**), resulting in an average size of 20 nm. The IrO_x nanoparticles deposited on TiN, denoted as IrO_x/TiN NPs, were achieved via a one-pot ethanol reduction approach with 30 wt. % of Ir loading. The transmission electron microscopy (TEM) images (**Figure 4a, 4b**) show the formation of IrO_x nanoparticles deposited on TiN NPs, and the IrO_x nanoparticles with the average size of 1.38 nm are uniformly dispersed on TiN NPs. The lattice distance of 0.223 nm is observed in **Figure 4c**, which can be attributed to the (111) crystalline plane of cubic Ir. The lattice distance of 0.243 nm corresponds to the (111) plane of cubic TiN. High-angle annular dark-field scanning TEM (HAADF-STEM) and X-ray energy dispersive spectroscopy (X-EDS) mapping (**Figure 4d**) reveal the coexistence of Ir, Ti, N, and O elements in IrO_x/TiN NPs. Moreover, X-EDS is used to determine the average Ir wt. % in the catalysts, and the results confirm that the final Ir loading matches well with the precursor ratio of 30 wt. % (**Table S3**). Powder X-ray diffraction (XRD) (**Figure S15**) is used to confirm the crystal structure and the phase properties of IrO_x/TiN NPs. A broad diffraction peak at $2\theta=41°$ is consistent with the presence of small Ir particles in the IrO_x/TiN. The peak feature of IrO_x/TiN NPs in XRD shows the metallic Ir with cubic crystal structure, consistent with the lattice distance measured in **Figure 4c**. Additionally, other diffraction peaks at $\theta=37.1, 43.1, 62.6, 75.1$, and 79.0° in the XRD pattern match well with the face-centered cubic structure of TiN.

XPS and X-ray absorption near-edge structure (XANES) were employed to analyze the chemical states of IrO_x/TiN NPs, Ir/C, and C-IrO_2. The Ir 4f XPS spectrum of IrO_x/TiN

NPs (**Figure 5a**) shows two peaks at 60.4 and 61.1 eV, which are attributed to Ir^0 and Ir^{4+}, respectively, indicating that the IrO_x/TiN catalyst contains a mixed oxidation state of Ir. In addition, the peaks shift to higher binding energy compared to that of the Ir foil, indicating that the Ir in IrO_x/TiN possesses a more positive oxidation state as well as the possible electronic interaction between IrO_x and the TiN support. The Ti 2p XPS spectrum of IrO_x/TiN (**Figure S16**) can be deconvoluted into two peaks at 456 and 458.3 eV, which are attributed to TiN/TiON and TiO_2, respectively, suggesting that the TiN surface is partially oxidized, likely due to the exposure of the catalyst to air during sample preparation for characterization. The Ir oxidation state in IrO_x/TiN can be further identified by XANES from the white line intensity in the XANES profile. As depicted in **Figure 5b**, the Ir L_3-edge XANES spectrum shows that the white line intensity for IrO_x/TiN falls between that of the C-IrO_2 and Ir/C standards, indicating a mixed oxidation state of Ir. This observation is consistent with conclusions from the XPS results. Furthermore, Ti K-edge XANES spectra (**Figure 5c**) indicate that the chemical state of Ti in IrO_x/TiN NPs is between the Ti foil (Ti^0) and TiO_2 (Ti^{4+}) standards.

The Fourier transform spectrum of phase-uncorrected extended X-ray absorption fine structure (EXAFS) of IrO_x/TiN NPs at Ir L_3-edge (**Figure 5d**) shows a prominent peak corresponding to the Ir-O shell. Another minor peak at 2.7 Å can be attributed to the metallic Ir-Ir, suggesting that IrO_x/TiN NPs contain a mixed oxidation state. The coordination environment is then confirmed by wavelet transform (WT) to compare the Ir L_3-edge between different samples (**Figure 5e**). The WT analysis of IrO_x/TiN NPs shows a maximum intensity at R=1.6 Å, k=4.9 $Å^{-1}$, close to the intense peak in the C-IrO_2 profile. A relatively weak peak is also observed at R=2.7 Å, k=8.8 $Å^{-1}$, corresponding to the Ir-Ir bond observed in the Ir/C profile. The observations from the EXAFS results match well with the findings from the XANES measurements.

The combined XPS, XANES, and EXAFS results suggest that Ir in IrO_x/TiN is a mixed oxidation state containing both metallic Ir and oxidized Ir. This is consistent with the DFT-optimized structures, showing that the IrO_x/TiN systems consist of the mixed $Ir^{\delta+}$/Ir^0 states (**Figure 1**). In addition, the coexistence of Ir-O, Ir-Ir, and Ir-Ti bonds is also observed by the theoretical models at the IrO_x-TiN interface.

2.4 Electrochemical OER performance of IrO_x/TiN nanoparticles in acidic electrolyte

The OER performance of IrO_x/TiN NPs and benchmark C-IrO_2 was evaluated in O_2-saturated 0.1 M $HClO_4$ electrolyte

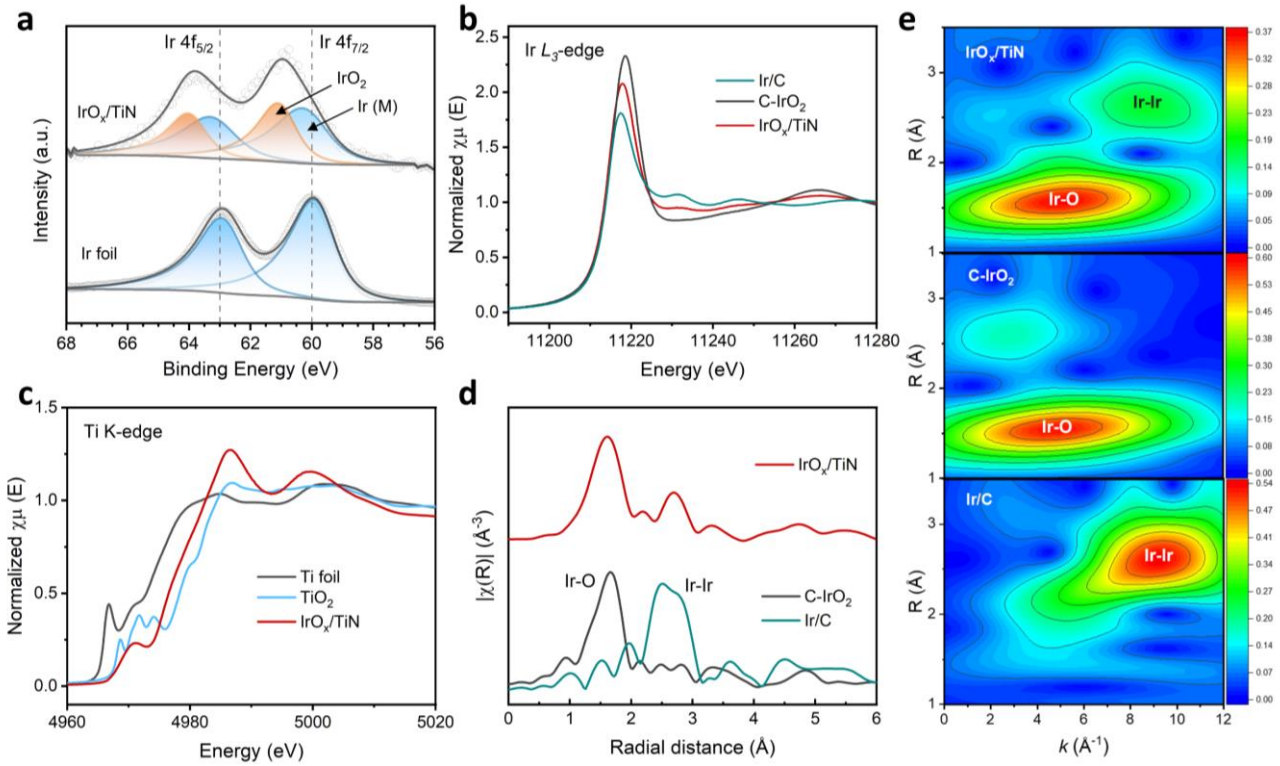

Figure 5. Electronic structure of IrO_x/TiN NPs, C-IrO_2 and Ir/C. a) Ir 4f XPS spectra; b) XANES spectra at the Ir L_3-edge. c) XANES spectra at the Ti K-edge of IrO_x/TiN NPs, Ti foil, and TiO_2 standards. d) The Ir L_3-edge k^2-weighted Fourier transform spectra. e) WT of the Ir L_3-edge for IrO_x/TiN NPs, C-IrO_2, and Ir/C.

on a rotating disk electrode (RDE) set-up. The current densities of the catalysts were normalized to the geometric area of the glassy carbon electrode (GCE). Linear sweep voltammetry (LSV) curves (**Figure 6a**) show that IrO_x/TiN catalysts with different Ir loadings of 40 and 60 μg_{Ir} cm^{-2} exhibit higher OER activity than C-IrO_2 (60 μg_{Ir} cm^{-2}). The overpotentials of IrO_x/TiN NPs with 40 and 60 μg of Ir correspond to 306 and 293 mV at 10 mA cm^{-2}, respectively, much lower than that of C-IrO_2 (337 mV). Under the same Ir loading, IrO_x/TiN NPs show a Tafel slope of 40.8 mV dec^{-1}, indicating this catalyst has faster kinetics than C-IrO_2 (52.1 mV dec^{-1}) (**Figure 6b**). To evaluate their intrinsic activity, the mass activity was calculated based on the Ir mass loading at the electrode. From **Figure 6c** and **Figure S17**, one can observe that the mass activities at 1.54 V are 270.8 A g_{Ir}^{-1} (40 μg_{Ir} cm^{-2}), 267.5 A g_{Ir}^{-1} (60 μg_{Ir} cm^{-2}) for IrO_x/TiN and 80.1 A g_{Ir}^{-1} (60 μg_{Ir} cm^{-2}) for C-IrO_2. Overall, the IrO_x/TiN catalysts exhibit mass activity approximately 3-fold higher than C-IrO_2 (**Figure S18).**

The OER stability of the IrO_x/TiN NPs and C-IrO_2, supported on carbon paper, was evaluated in 0.1 M $HClO_4$ by the chronopotentiometry method at a constant current density of 10 mA cm^{-2}. In **Figures 6d and S19**, IrO_x/TiN NPs maintain a stable potential for 250 hours of continuous operation, with only 29 mV overpotential increase (red dotted curves) at a potential degradation of 0.12 mV/h. In contrast, C-IrO_2 shows rapid degradation of its catalytic activity after 80 hours in the acidic electrolyte (**Figure S20**), likely due to the instability of the carbon paper substrate. Additionally, the dissolution of Ir from IrO_x/TiN and C-IrO_2 in the electrolyte was evaluated by ICP-OES after a 10-hour OER stability test. The results indicated that only trace amounts of Ir were detected (**Table S4**). Specifically, the amount of dissolved Ir for C-IrO_2 was 1.3 μg cm^{-2}, representing approximately 0.7% of Ir loss. In comparison, the dissolved Ir in the electrolyte for IrO_x/TiN was 0.56 μg cm^{-2}, resulting in only 0.3% of Ir loss during the stability test. This low Ir dissolution rate further demonstrated that the stability of IrO_x/TiN was comparable to or slightly better than C-IrO_2. Moreover, the activity of IrO_x/TiN catalysts at a high current density of 50 mA cm^{-2} remains relatively stable for 10 hours, although the stability is impacted by the fact that the carbon paper substrate suffers from thermodynamic instability and degrades under harsh acidic, oxidizing OER conditions (**Figure S21**). Overall, the IrO_x/TiN NPs show an excellent OER stability and enhanced activity when compared to Ir-based electrocatalysts reported in the literature (**Figure 6e** and **Table S5**) [27, 33-52].

Finally, the performance of IrO_x/TiN NPs and C-IrO_2 as anode catalysts under the same Ir loading (0.2 mg cm^{-2}) was evaluated in a PEMWE cell. In **Figures 6f**, the polarization

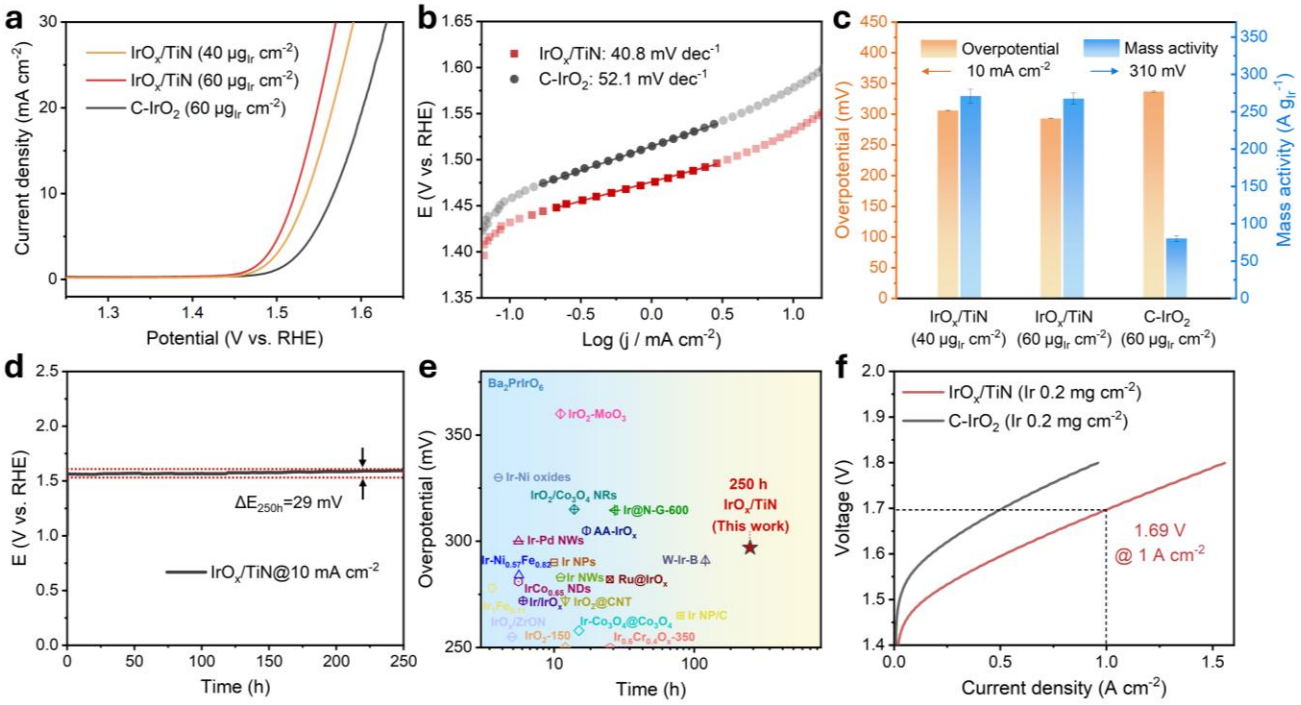

Figure 6. Electrochemical OER performances of IrO_x/TiN NPs and C-IrO_2 in 0.1 M $HClO_4$. a) LSV curves; b) Tafel plots. c) Comparison of overpotential and mass activity of C-IrO_2 and IrO_x/TiN NPs with various Ir loading at 1.54 V. d) Stability test of IrO_x/TiN NPs at a constant current density of 10 mA cm^{-2}. e) Comparison of the stability of IrO_x/TiN in acidic electrolyte with that of reported Ir-based catalysts. f) Polarization curves of PEMWEs using IrO_x/TiN and C-IrO_2 anodes in 0.1 M $HClO_4$ at 60 °C with Nafion NR-212 membrane.

curve reveals that the IrO_x/TiN catalyst demonstrates improved PEMWE activity compared to C-IrO_2. Specifically, PEMWE using IrO_x/TiN requires cell voltages of only 1.59 and 1.69 V to achieve a current density of 0.5 and 1 A cm^{-2}, respectively, much lower than those of C-IrO_2 (1.70 and above 1.8 V, respectively). The catalyst stability was evaluated at a constant current density of 100 mA cm^{-2} in 0.1 M $HClO_4$ at 60 °C (**Figure S22**). PEMWE with both C-IrO_2 and IrO_x/TiN anodes at a low Ir loading of 0.2 mg cm^{-2} exhibits a similar stability, with a relatively small voltage increase of 44 mV over 40 hours. However, the PEMWE cell using the IrO_x/TiN anode can be operated at lower voltage (1.49 V), indicating better activity compared to C-IrO_2 (1.58 V).

2.5 *In situ* characterization of IrO_x/TiN nanoparticles during OER

The chemical state of Ir and its interaction with the TiN support were further probed by *in situ* XANES and EXAFS, using a homemade *in situ* electrochemical cell (**Figure 7a**). *In situ* XANES offers insight on the dynamic changes in the oxidation state of the IrO_x/TiN NPs during acidic OER at various applied potentials in the order of 0.4 V, 1.32 V, 1.54 V, 1.65 V, and then back to 0.4 V. As shown in **Figure 7b**, the XANES peaks gradually shift toward higher energy with an increase in the applied potentials from 0.4 to 1.65 V, accompanied by an increase in the white line intensity, which may be attributed to the gradual increase of the Ir oxidation state as well as the formation of various oxygen-containing intermediates (i.e., O*, OH*, OOH*) adsorbing on the metal surface during the OER process[53]. The Ir L_3-edge XANES profiles of Ir/C, C-IrO_2, and IrO_x/TiN at the increased applied potentials from 0.4 V to 1.65 V, and then back to 0.4 V, are shown in **Figures 7c-g**, and the comparison of their white

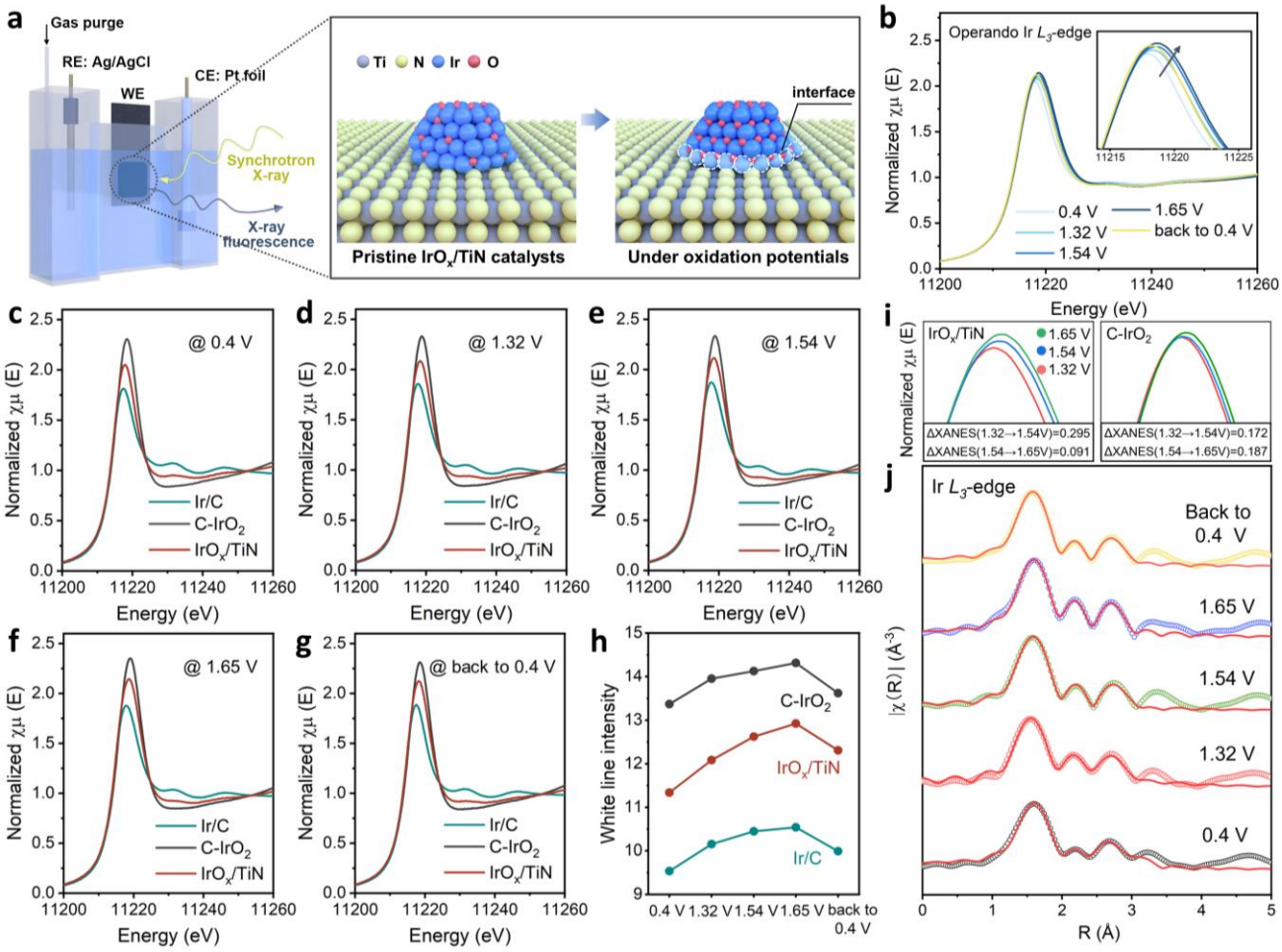

Figure 7. The Fourier-transformed EXAFS spectra and corresponding fitting plots in R space at various applied potentials. a) Schematic illustration of the *in situ* H-cell experimental set-up and the structure evolution of IrO_x/TiN NPs before and during the OER measurement. b) *In situ* Ir L_3-edge XANES spectra of IrO_x/TiN NPs. c-g) Ir L_3-edge XANES spectra of IrO_x/TiN NPs, Ir/C, and C-IrO_2 at various potentials. h) The change in the white line intensity of IrO_x/TiN NPs, Ir/C, and C-IrO_2. i) The differences of the white line intensity between 1.32 and 1.54 V, and 1.54 and 1.65 V on IrO_x/TiN NPs and C-IrO_2. j) Ir L_3-edge EXAFS spectra (points) and curve fits (lines) for IrO_x/TiN at various potentials.

line intensities are plotted in **Figure 7h.** One can observe that the white line intensity of IrO_x/TiN increases with increasing applied potential and reaches its highest intensity at 1.65 V. This intensity is very close to that of the pristine C-IrO_2, suggesting that the oxidation state of Ir in IrO_x/TiN is high and similar to IrO_2 under the acidic OER conditions. A similar trend of the white line intensity change also appears in the reference compounds of C-IrO_2 and Ir/C XANES spectra (**Figure 7h** and **Figure S23**). According to *in situ* Ti K-edge XANES profiles of IrO_x/TiN NPs, no obvious shift of the edge feature occurs (**Figure S24**), indicating that TiN possesses excellent resistance to acid corrosion and oxidation during the OER process.

EXAFS fitting results of IrO_x/TiN NPs (**Figure 7j, Figure S25, S26** and **Table S6**) show the Ir-O bond length of 1.99 Å with an average coordination number (CN) of 2.7±0.6. The CN of IrO_x/TiN is much smaller than that of Ir-O (4.9±0.8) in the C-IrO_2 standard (**Figure S27, S28** and **Table S7**), likely due to the unsaturated oxygen on the IrO_x/TiN surface and the ultrasmall size of IrO_x. A peak in the IrO_x/TiN EXAFS profile with a bond length of 2.95 Å was observed at the potential of 1.32 V and above. Different from the Ir-Ir bond length of 2.70 Å, this peak with longer bond length can be attributed to the formation of the Ir-Ti bond at the interface. The EXAFS fitting reveals the Ir-Ti CN values to be 0.52±0.5, 0.79±0.5, and 0.82±0.5 at potentials of 1.32 V, 1.54 V, and 1.65 V, respectively. Even after reducing the potential back to 0.4 V, the Ir-Ti bond still exists, suggesting that the Ir-Ti bond remains stable after its formation at oxidizing potentials. The Ir-Ti bond can also be elucidated through XANES results. In the IrO_x/TiN XANES results (**Figure 7i**), there is a noticeable disparity in the white line intensity (ΔXANES) between 1.32 V and 1.54 V, with a difference of 0.295, but this difference sharply decreased to 0.091 upon increasing the potential from 1.54 V to 1.65 V. In contrast, in the C-IrO_2 XANES profile, the white line intensity difference between 1.32 V and 1.54 V is 0.172 and slightly increases to 0.187 when the potential increases from 1.54 V to 1.65 V. This observation suggests that IrO_x/TiN NPs under high oxidation potentials exhibit strong orbital hybridization at the interface, leading to enhanced alloying between Ir and Ti, thereby suppressing the increased white line intensity. Overall, the *in situ* XAS analyses reveal a strong metal-support interaction between the IrO_x NPs and the TiN support during the OER, consistent with the DFT results. The overlayer models in DFT calculations and thin films/NPs in experimental studies share the same active sites, the high-coordinated IrO_x terrace sites. Upon going from 1ML-IrO_x/TiN to 3ML-IrO_x/TiN, more electron transfer from TiN via Ir-Ti bond is observed to moderate *OH binding on the supported IrO_x overlayer and promote the OER activity, while Ir at the interface is less oxidized to strengthen Ir-Ti interaction and ensure stability of IrO_x overlayer in the acidic OER environment (**Figures S29** and **S30**).

3. CONCLUSIONS

In summary, we have demonstrated a framework for designing active and stable catalysts for acidic OER based on DFT predictions and experimental verification using thin films and nanoparticles. DFT calculations predict that IrO_x/TiN should possess a better OER activity compared to IrO_x catalysts alone, which is attributed to the interaction with TiN. Using the adsorption energy of *OH as the descriptor, the OER activity is improved by increasing the number of Ir layers over TiN, which is verified by experimentally-synthesized IrO_x/TiN thin films. Encouraged by the promising thin film results, the commercially viable powder catalysts of IrO_x/TiN NPs were synthesized, yielding a low overpotential of 293 mV, high mass activity of 270.8 A g_{Ir}^{-1} at 1.54 V, and excellent stability after 250 h operation at 10 mA cm^{-2}. When the IrO_x/TiN catalyst was used in a PEMWE cell with a low Ir loading of 0.2 mg cm^{-2}, it required a lower voltage (1.69 V) compared to C-IrO_2 (>1.8 V) to achieve a current density of 1 A cm^{-2}. *In situ* XAS results further revealed that this enhanced OER performance could be attributed to the interaction between IrO_x and TiN under the acidic OER conditions. This study highlights a framework to enable effective catalyst discovery, going from theory-guided DFT prediction, experimental verification over well-characterized thin films, to the development of high-performance powder electrocatalysts.

4. Theoretical and Experimental Methods

4.1 Computational methods

All density functional theory calculations were performed using the Vienna Ab initio Simulation Package[54, 55] (VASP), interfaced with the Atomic Simulation Environment[56]. The ion-electron interactions were described by the projector-augmented wave pseudopotentials. The revised Perdew-Burke-Ernzerhof generalized gradient approximation[57] was selected to describe the exchange and correlation interactions. The cutoff energy was 500 eV for plane-wave basis sets with Fermi-level smearing of 0.05 eV for slabs and 0.01 eV for gas species. In this work, six model systems were computed, including 1ML-IrO_x/TiN overlayer, 2ML-IrO_x/TiN overlayer, 3ML-IrO_x/TiN overlayer, IrO_x/TiN interface, 1ML-IrO_x, and 2ML-IrO_x. For the TiN support, TiN was represented by 2 layers of a 3 × 3 supercell with a lattice parameter of a = b = c = 4.248 Å. For the 1ML-IrO_x/TiN overlayer, one monolayer of *O was adsorbed at the hollow site of Ir(111) to mimic the partial oxidation state. For the 2ML-IrO_x/TiN overlayer, one monolayer of surface *O and one mono-sublayer *O were used. The sublayer *O was placed at the tetrahedral sites, which denoted the type of site with three Ir atoms above the *O and one Ir atom below.[58] For the 3ML-IrO_x/TiN overlayer, the same *O setup was used compared to the 2ML-IrO_x/TiN overlayer. The only difference between 2ML-IrO_x/TiN and 3ML-IrO_x/TiN was that 3ML-IrO_x/TiN had two metallic Ir layers underneath the oxidized IrO_x layer. For the IrO_x/TiN interface, a cluster of 16 Ir atoms and 25 O atoms was constructed over the TiN. The cluster was constructed to ensure all exposed Ir atoms were fully oxidized. For 1ML-IrO_x and 2ML-IrO_x, both were constructed by four layers of Ir(111) of a 4 × 4 supercell with a lattice parameter of a = b = c = 3.85 Å. The corresponding *O layers had the same configuration as TiN-supported models. IrO_2(110), denoted as IrO_2, was also included as a reference (**Figure S1**). The adsorbates and top two layers,

including IrO_x, were fully relaxed until the energy and interatomic forces were minimized down to 1×10^{-5} eV and 0.03 eV/Å, respectively. The bottom two layers were fixed in their bulk positions. The slab was separated with 20 Å of vacuum space to avoid interactions in the periodic calculations in the z-direction. All DFT energies were corrected by the zero-point energy and entropic contributions, and details can be found in **SI** and **Table S1**. Note that the current theoretical model did not include the effects that could be introduced by solvation and surface charge, as reported previously. [59, 60] However, previous studies without considering these effects demonstrated agreement between DFT-predicted the trend in OER activity of metal oxides and that observed experimentally. [61, 62] Here, the solvation effect was described by depositing one bilayer of explicit water molecules in an ice-like matrix on the (111)-like IrO_x/TiN overlayer, which was allowed to fully relax (**Figure S9**). The hexagonal water matrix was optimized, resulting in half of the water molecules pointed down to form hydrogen bonds with the chemisorbed *O on the surface, while the ice-like bilayer structure remained in general. According to a previous computational study, the catalytic behavior predicted using this type of model was in good agreement with the experimental measurements for the oxygen reduction reaction over Pt(111).[63] The results showed that the absolute values of OER overpotentials vary due to the solvation effect, but the predicted trend in OER overpotential, 1ML-IrO_x/TiN > 2ML-IrO_x/TiN > 3ML-IrO_x/TiN, remains the same, in good agreement with the experimental results (**Figures 3c** and **S10**).

4.2 Synthesis Electrocatalysts

4.2.1 Chemicals

Hydrogen hexachloroiridate (IV) hexahydrate ($H_2IrCl_6 \cdot 6H_2O$) was purchased from Fisher Scientific. Commercial iridium oxide (C-IrO_2, 99%), perchloric acid ($HClO_4$), and hydrochloric acid (HCl) were purchased from Thermo Fisher Scientific. Sodium hydroxide (NaOH), titanium chloride ($TiCl_4$, 99.9%), titanium foil (Ti foil, 99.7%), Nafion perfluorinated resin solution (10 wt%), anhydrous chloroform, acetone, anhydrous ethanol, and isopropanol were purchased from Sigma Aldrich. The AvCarb carbon paper was purchased from FuelCellStore. Ar (99.999%), O_2 (99.99), and NH_3 (99.995%) gases were purchased from Praxair Inc. All the chemicals and commercial catalysts were used as received without further treatment/purification.

4.2.2 Preparation of IrO_x/TiN films

TiN thin films were prepared by using 0.127 mm thick Ti foils. The foils were washed by ultrasonication in ethanol for 10 minutes for surface cleaning and then air-dried. Subsequently, the cleaned Ti foils were placed into a horizontal tube furnace for nitridation. After purging with Ar for 15 minutes at 200 standard cubic centimeters per minute (sccm), the gas was switched to NH_3 with a flow rate of 150 sccm. The temperature ramped from 25 °C to 750 °C in 2 hours and held at 750 °C for 10 hours. After that, TiN was cooled under NH_3 until it reached room temperature. The TiN thin films were collected for further use.

The Ir deposition was performed in an ultra-high vacuum XPS (UHV-XPS) instrument with a base pressure of 1×10^{-9} Torr. The introduction of Ir to as-prepared TiN films was accomplished through physical vapor deposition using a commercially available (Focus EFM 3T) e-Beam evaporator. Typically, an iridium rod (Thermo Fisher Scientific Chemicals, 1.0mm dia, 99.8%) was placed in one of the three pockets of the EFM 3T evaporator. Ir evaporation occurred by heating the rod near its melting point, maintaining a constant flux rate of approximately 6 nA (HV = 950 V, Iemis. = 17.1 mA, Ifil. = 2.35 A) for 1 to 3 hours based on coverage. The Ir overlayer on the TiN film was then annealed at 600 K for 20 minutes in the presence of 5.0×10^{-7} Torr O_2 to further oxidize Ir. Finally, XPS results were utilized for the calculation of Ir coverage.

4.2.3 Preparation of IrO_x/TiN NPs

The $TiCl_4$ was dissolved in anhydrous chloroform inside a glove box. [32] The mixture was stirred for an hour and then connected to a Schlenk line with the anhydrous NH_3 gas purging. The dissolved $TiCl_4$ reacted with NH_3 gas with a flow rate of 100 sccm for 10 hours. Subsequently, the mixture was heated to 100 °C to evaporate all the solvent. The as-prepared powders were collected and transferred into a quartz boat, which was then placed into a tube furnace to heat at a rate of 5 °C/min and held at 750 °C for 10 hours under an NH_3 gas flow. After cooling to room temperature, the TiN NPs were collected and treated with 10 % hydrochloric acid for surface cleaning. The acid-treated TiN NPs were collected by centrifugation, washed twice with DI water, and dried in a vacuum oven at 60 °C overnight.

$H_2IrCl_6 \cdot 6H_2O$ was dissolved in anhydrous ethanol and then heated in an oil bath for an hour, changing the solution color from dark brown to light yellow. [64, 65] A certain amount of the ethanolic $H_2IrCl_6 \cdot 6H_2O$ solution was mixed with acid-treated TiN NPs. The mixture was sonicated for 5 minutes, stirred for 10 minutes, and then 0.5 M NaOH solution was added. The solution was refluxed at 80 °C for 2 hours with vigorous stirring under the Ar flow. After cooling to room temperature, the IrO_x/TiN NPs were filtered and washed with deionized water using vacuum filtration. The obtained powder was vacuum-dried at 40 °C overnight.

4.3 Material Characterization

X-ray powder diffraction (XRD) was collected by a Rigaku Miniflex II with Cu Kα radiation with a sweep rate of 5° min^{-1} from 10° to 80°. The size and morphology of catalysts were characterized by transmission electron microscopy (TEM) (JEM-1400). High-angle annular dark-field scanning TEM (STEM-HAADF) and X-ray energy dispersive spectroscopy (X-EDS) were conducted on FEI Talos 200× TEM at an accelerating voltage of 200 kV at Brookhaven National Laboratory. X-ray photoelectron spectroscopy (XPS) measurements on both the powder and film samples were conducted at the Chemistry Department of Brookhaven National Laboratory. For the powder sample, the analysis employed a commercial SPECS AP-XPS chamber featuring a

PHOIBOS 150 EP MCD-9 analyzer and an X-ray source with an Al Kα anode, focusing on recording the Ti 2p, Ir 4d, Ir 4f, O 1s, N 1s and C 1s regions. For the film sample, XPS analysis utilized a VG Scienta SES 100 analyzer and an X-ray source featuring an Al Kα anode. The focus was on recording the Ti 2p, Ir 4d, Ir 4f, O 1s, N 1s, and C 1s regions.

The X-ray absorption spectroscopy (XAS) for Ir L_3-edge and Ti K-edge were collected at beamline 7-BM (QAS) of the National Synchrotron Light Sources II (NSLS-II) at Brookhaven National Laboratory. The Ir L_3-edge and Ti K-edge spectra were obtained in a fluorescence mode using a passivated implanted planar silicon (PIPS) detector. Typically, the IrO_x/TiN ink was coated on carbon black (1×1 cm^2) with an Ir mass loading of 0.5 mg cm^{-2} as the working electrode and put into the home-made acryl *in situ* H-type cell. [66] The data were recorded under different applied potentials of 0.4, 1.32, 1.54, 1.65, and 0.4 V vs. RHE. The duration for a single spectrum was around 1 minute, and fifteen spectra were merged to improve the signal-to-noise ratio. Ir and Ti foils, as the standard references, were employed to calibrate energy shifts and obtain the passive electron reduction factor ($S0^2$) used for the extended X-ray absorption fine structure (EXAFS) fitting. All the data processing was conducted using the IFEFFIT package.

4.4 Electrochemical Measurements

All electrochemical OER measurements were carried out in a conventional three-electrode cell at room temperature with a CHI electrochemical workstation. The IrO_x/TiN (3.92 mg) was dispersed in 992.2 µL solution of 3:1 v/v of water: isopropanol with 7.8 µL of Nafion (perfluorinated resin, 10 wt. % in H_2O), and the ink was obtained by ultrasonication for 1 hour to form a homogeneous solution. 10 µL of ink were dropped on glassy carbon electrode (GCE) of 5 mm in diameter and naturally dried in ambient air, achieving the Ir mass loading of 60 μg_{Ir} cm^{-2}. To avoid passivation of GCE, carbon fiber paper loaded with IrO_x/TiN catalyst was used as a working electrode for the long-term stability test, and the catalyst loading was 200 μg_{Ir} cm^{-2}. A platinum foil was used as a counter electrode, while an Ag/AgCl in 3.5 M KCl was used as a reference electrode. The Ag/AgCl electrode was calibrated with a hydrogen electrode (EDAQ, HydroFlex) before electrochemical measurements. Linear sweep voltammetry (LSV) curves were conducted in an O_2-saturated 0.1 M $HClO_4$ solution at 10 mV s^{-1} with a rotation rate of 1600 rpm. Tafel slope tests were conducted with scan rate of 1 mV s^{-1}. The stability tests were performed at 10 mA cm^{-2} and 50 mA cm^{-2}, respectively. Inductively coupled plasma optical emission spectroscopy (ICP-OES) was used to determine the dissolution of Ir after the stability test. All the potential was controlled by *iR*-compensation (95%) and converted to the reversible hydrogen electrode (RHE).

4.5 PEMWE operation

Commercial Pt/C (46.9%) (TKK) were utilized as the cathode catalyst. Commercial IrO_2 (Thermo Fisher Scientific) and IrO_x/TiN NPs were tested as the catalysts for the anode. The preparation of the cathode ink involved using 32 mg of the catalyst, to which 320 µL of water was added, followed by 15 mL of isopropyl alcohol (IPA). Nafion D521 ionomer solutions (5 wt. % in H_2O/IPA blend, Ion Power) were then mixed into the cathode ink and homogenized through sonication for 30 minutes. Spectracarb 2050A-1535 (381 µm, CP, Spectracarb) was utilized as the porous transport layer (PTL) for both the anode and cathode. The Pt/C catalyst ink was applied to acid-prepared Nafion NR-212 (50.8 µm, Ion Power) membranes by spray coating, achieving a catalyst loading of 1 mg_{Pt} cm^{-2}. The same preparation method was applied to the Ir-based anode catalyst ink, with a catalyst loading of 0.2 mg_{Ir} cm^{-2} on PTL. Graphite single serpentine flow fields were used for both the cathode and anode. To prevent electrolyte leakage and minimize electrical resistance between the membrane electrode assembly (MEA), a gasket (230 µm) was installed between the membrane and the flow field. All components were assembled in a 5 cm^2 electrolyzer (Scribner), and the assembly was secured using a torque wrench set to 10 N·m. 0.1 M $HClO_4$ electrolyte (60°C) was circulated through the anode using a peristaltic pump (Cole-Palmer) and PTFE tubing, while degassed hydrogen and oxygen were vented. A potentiostat equipped with a booster (VSP with a VMP3B-20 20 A booster, Biologic) was employed to conduct current-voltage (I-V) measurements and chronopotentiometry to assess the performance of the MEA.

ASSOCIATED CONTENT

Supporting Information. Additional DFT calculation results, characterizations, electrochemical data, XANES profiles, EXAFS fitting results, and tables.

AUTHOR INFORMATION

Corresponding Authors

Jingguang G. Chen - Chemistry Division, Brookhaven National Laboratory, Upton, New York 11973, United States; Department of Chemical Engineering, Columbia University, New York, New York 10027, United States.
Orcidhttps://orcid.org/0000-0002-9592-2635.
Email: jgchen@columbia.edu
Ping Liu - Chemistry Division, Brookhaven National Laboratory, Upton, New York 11973, Unite States.
Orcidhttps://orcid.org/0000-0001-8363-070X.
Email: pingliu3@bnl.gov

Authors

Xue Han - Chemistry Division, Brookhaven National Laboratory, Upton, New York 11973, Unite States.
Tianyou Mou - Chemistry Division, Brookhaven National Laboratory, Upton, New York 11973, Unite States.
Arephin Islam - Chemistry Division, Brookhaven National Laboratory, Upton, New York 11973, Unite States.
Sinwoo Kang - Department of Chemical Engineering, Columbia University, New York, New York 10027, United States.
Qiaowan Chang - School of Chemical Engineering and Bioengineering, Washington State University, Pullman, WA 99164-6515, Unite States.

Zhenhua Xie - Department of Chemical Engineering, Columbia University, New York, New York 10027, United States.
Xueru Zhao - Chemistry Division, Brookhaven National Laboratory, Upton, New York 11973, Unite States.
Kotaro Sasaki - Chemistry Division, Brookhaven National Laboratory, Upton, New York 11973, Unite States.
José A. Rodriguez - Chemistry Division, Brookhaven National Laboratory, Upton, New York 11973, Unite States.

Author Contributions

‡These authors contributed equally.

Notes

These authors declare no competing financial interest.

ACKNOWLEDGMENT

This work was financially supported by the Division of Chemical Sciences, Geosciences, & Biosciences, Office of Basic Energy Sciences, Department of Energy, Grant number DE-SC0012704 (BNL FWP CO-060). This research used resources of the Center for Functional Nanomaterials (CFN) and beamlines 7-BM (QAS) of the National Synchrotron Light Source II (NSLS-II) at Brookhaven National Laboratory (Contract No. DE-SC0012704 and DE-SC0012653), U.S. DOE Office of Science User Facilities. Beamline operations were supported in part by the Synchrotron Catalysis Consortium (U.S. DOE, Office of Basic Energy Sciences, Grant No. DE-SC0012335). DFT calculations in this work were performed using computational resources at Center for Functional Nanomaterials (CFN), and the Scientific Data and Computing Center, a component of the Computational Science Initiative, at Brookhaven National Laboratory under Contract No. DE-SC0012704, and at the National Energy Research Scientific Computing Center (NERSC), a DOE Office of Science User Facility, supported by the Office of Science of the DOE under contract DE-AC02-05CH11231. We thank Dario Lewczyk and Prof. Peter Khalifah for preparing the TiN films, and Samay Garg for performing the ICP measurements.

REFERENCES

(1) Chen, F.-Y.; Wu, Z.-Y.; Adler, Z.; Wang, H. Stability challenges of electrocatalytic oxygen evolution reaction: From mechanistic understanding to reactor design. *Joule* **2021**, *5* (7), 1704-1731. DOI: https://doi.org/10.1016/j.joule.2021.05.005.
(2) Shi, Q.; Zhu, C.; Du, D.; Lin, Y. Robust noble metal-based electrocatalysts for oxygen evolution reaction. *Chemical Society Reviews* **2019**, *48* (12), 3181-3192.
(3) Roger, I.; Shipman, M. A.; Symes, M. D. Earth-abundant catalysts for electrochemical and photoelectrochemical water splitting. *Nature Reviews Chemistry* **2017**, *1* (1), 0003. DOI: 10.1038/s41570-016-0003.
(4) Tackett, B. M.; Sheng, W.; Kattel, S.; Yao, S.; Yan, B.; Kuttiyiel, K. A.; Wu, Q.; Chen, J. G. Reducing Iridium Loading in Oxygen Evolution Reaction Electrocatalysts Using Core–Shell Particles with Nitride Cores. *ACS Catalysis* **2018**, *8* (3), 2615-2621. DOI: 10.1021/acscatal.7b04410.
(5) Song, J.; Wei, C.; Huang, Z.-F.; Liu, C.; Zeng, L.; Wang, X.; Xu, Z. J. A review on fundamentals for designing oxygen evolution electrocatalysts. *Chemical Society Reviews* **2020**, *49* (7), 2196-2214, 10.1039/C9CS00607A. DOI: 10.1039/C9CS00607A.
(6) Dang, Q.; Lin, H.; Fan, Z.; Ma, L.; Shao, Q.; Ji, Y.; Zheng, F.; Geng, S.; Yang, S.-Z.; Kong, N.; et al. Iridium metallene oxide for acidic oxygen evolution catalysis. *Nature Communications* **2021**, *12* (1), 6007. DOI: 10.1038/s41467-021-26336-2.
(7) Feng, J.; Dong, Z.; Ji, Y.; Li, Y. Accelerating the Discovery of Metastable IrO_2 for the Oxygen Evolution Reaction by the Self-Learning-Input Graph Neural Network. *JACS Au* **2023**, *3* (4), 1131-1140. DOI: 10.1021/jacsau.2c00709.
(8) Galyamin, D.; Tolosana-Moranchel, Á.; Retuerto, M.; Rojas, S. Unraveling the Most Relevant Features for the Design of Iridium Mixed Oxides with High Activity and Durability for the Oxygen Evolution Reaction in Acidic Media. *JACS Au* **2023**, *3* (9), 2336-2355. DOI: 10.1021/jacsau.3c00247.
(9) Kasian, O.; Grote, J.-P.; Geiger, S.; Cherevko, S.; Mayrhofer, K. J. J. The Common Intermediates of Oxygen Evolution and Dissolution Reactions during Water Electrolysis on Iridium. *Angewandte Chemie International Edition* **2018**, *57* (9), 2488-2491. DOI: https://doi.org/10.1002/anie.201709652.
(10) Ge, S.; Xie, R.; Huang, B.; Zhang, Z.; Liu, H.; Kang, X.; Hu, S.; Li, S.; Luo, Y.; Yu, Q.; et al. A robust chromium–iridium oxide catalyst for high-current–density acidic oxygen evolution in proton exchange membrane electrolyzers. *Energy & Environmental Science* **2023**, *16* (9), 3734-3742, 10.1039/D3EE01192E. DOI: 10.1039/D3EE01192E.
(11) Shan, J.; Ye, C.; Chen, S.; Sun, T.; Jiao, Y.; Liu, L.; Zhu, C.; Song, L.; Han, Y.; Jaroniec, M.; et al. Short-Range Ordered Iridium Single Atoms Integrated into Cobalt Oxide Spinel Structure for Highly Efficient Electrocatalytic Water Oxidation. *Journal of the American Chemical Society* **2021**, *143* (13), 5201-5211. DOI: 10.1021/jacs.1c01525.
(12) Wu, X.; Feng, B.; Li, W.; Niu, Y.; Yu, Y.; Lu, S.; Zhong, C.; Liu, P.; Tian, Z.; Chen, L.; et al. Metal-support interaction boosted electrocatalysis of ultrasmall iridium nanoparticles supported on nitrogen doped graphene for highly efficient water electrolysis in acidic and alkaline media. *Nano Energy* **2019**, *62*, 117-126. DOI: https://doi.org/10.1016/j.nanoen.2019.05.034.
(13) Hou, L.; Jang, H.; Liu, H.; Li, Z.; Kim, M. G.; Qin, Q.; Liu, X. Synergistic Effect of Electronic Particle–Support Interactions on the Ir-Based Multiheterostructure for Acidic Water Oxidation. *ACS Sustainable Chemistry & Engineering* **2022**, *10* (48), 15950-15957. DOI: 10.1021/acssuschemeng.2c05377.
(14) Tian, D.; Denny, S. R.; Li, K.; Wang, H.; Kattel, S.; Chen, J. G. Density functional theory studies of transition metal carbides and nitrides as electrocatalysts. *Chemical Society Reviews* **2021**, *50* (22), 12338-12376, 10.1039/D1CS00590A. DOI: 10.1039/D1CS00590A.
(15) Mou, H.; Jeong, J. J.; Lamichhane, B.; Kattel, S.; Zhuang, Z.; Lee, J. H.; Chang, Q.; Chen, J. G. Trends in electrocatalytic activity and stability of transition metal nitrides. *Chem Catalysis* **2024**, *4* (2), 100867. DOI: https://doi.org/10.1016/j.checat.2023.100867.
(16) Wang, H.; Li, J.; Li, K.; Lin, Y.; Chen, J.; Gao, L.; Nicolosi, V.; Xiao, X.; Lee, J.-M. Transition metal nitrides for electrochemical energy applications. *Chemical Society Reviews* **2021**, *50* (2), 1354-1390, 10.1039/D0CS00415D. DOI: 10.1039/D0CS00415D.
(17) Jamil, R.; Ali, R.; Loomba, S.; Xian, J.; Yousaf, M.; Khan, K.; Shabbir, B.; McConville, C. F.; Mahmood, A.; Mahmood, N. The role of nitrogen in transition-metal nitrides in electrochemical water splitting. *Chem Catalysis* **2021**, *1* (4), 802-854. DOI: https://doi.org/10.1016/j.checat.2021.06.014.
(18) Zhong, Y.; Xia, X.; Shi, F.; Zhan, J.; Tu, J.; Fan, H. J. Transition Metal Carbides and Nitrides in Energy Storage and Conversion. *Advanced Science* **2016**, *3* (5), 1500286. DOI: https://doi.org/10.1002/advs.201500286.
(19) Parveen, N.; Ansari, M. O.; Ansari, S. A.; Kumar, P. Nanostructured Titanium Nitride and Its Composites as High-Performance Supercapacitor Electrode Material. *Nanomaterials* **2023**, *13* (1), 105.

(20) Shin, H.; Kim, H.-i.; Chung, D. Y.; Yoo, J. M.; Weon, S.; Choi, W.; Sung, Y.-E. Scaffold-Like Titanium Nitride Nanotubes with a Highly Conductive Porous Architecture as a Nanoparticle Catalyst Support for Oxygen Reduction. *ACS Catalysis* **2016**, *6* (6), 3914-3920. DOI: 10.1021/acscatal.6b00384.
(21) Li, G.; Li, K.; Yang, L.; Chang, J.; Ma, R.; Wu, Z.; Ge, J.; Liu, C.; Xing, W. Boosted Performance of Ir Species by Employing TiN as the Support toward Oxygen Evolution Reaction. *ACS Applied Materials & Interfaces* **2018**, *10* (44), 38117-38124. DOI: 10.1021/acsami.8b14172.
(22) Karade, S. S.; Sharma, R.; Gyergyek, S.; Morgen, P.; Andersen, S. M. IrO_2/Ir Composite Nanoparticles (IrO_2@Ir) Supported on TiN_xO_y Coated TiN: Efficient and Robust Oxygen Evolution Reaction Catalyst for Water Electrolysis. *ChemCatChem* **2023**, *15* (4), e202201470. DOI: https://doi.org/10.1002/cctc.202201470.
(23) Zhang, K.; Mai, W.; Li, J.; Wang, H.; Li, G.; Hu, W. Highly scattered Ir oxides on TiN as an efficient oxygen evolution reaction electrocatalyst in acidic media. *Journal of Materials Science* **2020**, *55* (8), 3507-3520. DOI: 10.1007/s10853-019-04201-4.
(24) Turaczy, K. K.; Liao, W. J.; Mou, H. S.; Nichols, N. N.; Liu, P.; Chen, J. G. Correlating Experimentally Determined Hydrogen Binding Energy with Hydrogen Evolution Activity over Metal Monolayers on Molybdenum Nitride. *ACS Catalysis,* **2023**, *13* (21), 14268-14276. DOI: 10.1021/acscatal.3c04063.
(25) Buchinger, J.; Löfler, L.; Ast, J.; Wagner, A.; Chen, Z.; Michler, J.; Zhang, Z. L.; Mayrhofer, P. H.; Holec, D.; Bartosik, M. Fracture properties of thin film TiN at elevated temperatures. *Materials&Design* **2020**, *194*, 108885. DOI: 10.1016/j.matdes.2020.108885.
(26) Ping, Y.; Nielsen, R. J.; Goddard, W. A., 3rd. The Reaction Mechanism with Free Energy Barriers at Constant Potentials for the Oxygen Evolution Reaction at the IrO_2 (110) Surface. *Journal of the American Chemical Society,* **2017**, *139* (1), 149-155. DOI: 10.1021/jacs.6b07557.
(27) Lee, C.; Shin, K.; Park, Y.; Yun, Y. H.; Doo, G.; Jung, G. H.; Kim, M.; Cho, W.-C.; Kim, C.-H.; Lee, H. M.; et al. Catalyst-support interactions in Zr_2ON_2-supported IrO_x electrocatalysts to break the trade-off relationship between the activity and stability in the acidic oxygen evolution reaction. *Advanced Functional Materials,* **2023**, *33* (25), 2301557. DOI: https://doi.org/10.1002/adfm.202301557.
(28) Klyukin, K.; Zagalskaya, A.; Alexandrov, V. Ab Initio Thermodynamics of Iridium Surface Oxidation and Oxygen Evolution Reaction. *Journal of Physical Chemistry C* **2018**, *122* (51), 29350-29358. DOI: 10.1021/acs.jpcc.8b09868.
(29) Gu, X. K.; Camayang, J. C. A.; Samira, S.; Nikolla, E. Oxygen evolution electrocatalysis using mixed metal oxides under acidic conditions: Challenges and opportunities. *Journal of catalysis* **2020**, *388*, 130-140. DOI: 10.1016/j.jcat.2020.05.008.
(30) Yoo, J. S.; Rong, X.; Liu, Y. S.; Kolpak, A. M. Role of Lattice Oxygen Participation in Understanding Trends in the Oxygen Evolution Reaction on Perovskites. *ACS Catalysis* **2018**, *8* (5), 4628-4636. DOI: 10.1021/acscatal.8b00612.
(31) Man, I. C.; Su, H. Y.; Calle-Vallejo, F.; Hansen, H. A.; Martínez, J. I.; Inoglu, N. G.; Kitchin, J.; Jaramillo, T. F.; Norskov, J. K.; Rossmeisl, J. Universality in Oxygen Evolution Electrocatalysis on Oxide Surfaces. *Chemcatchem* **2011**, *3* (7), 1159-1165. DOI: 10.1002/cctc.201000397.
(32) Choi, D.; Kumta, P. N. Nanocrystalline TiN Derived by a Two-Step Halide Approach for Electrochemical Capacitors. *Journal of The Electrochemical Society* **2006**, *153* (12), A2298. DOI: 10.1149/1.2359692.
(33) Fu, L.; Zeng, X.; Cheng, G.; Luo, W. IrCo Nanodendrite as an Efficient Bifunctional Electrocatalyst for Overall Water Splitting under Acidic Conditions. *ACS Applied Materials & Interfaces* **2018**, *10* (30), 24993-24998. DOI: 10.1021/acsami.8b08717.
(34) Yi, L.; Feng, B.; Chen, N.; Li, W.; Li, J.; Fang, C.; Yao, Y.; Hu, W. Electronic interaction boosted electrocatalysis of iridium nanoparticles on nitrogen-doped graphene for efficient overall water splitting in acidic and alkaline media. *Chemical Engineering Journal* **2021**, *415*, 129034. DOI: https://doi.org/10.1016/j.cej.2021.129034.
(35) Li, R.; Wang, H.; Hu, F.; Chan, K. C.; Liu, X.; Lu, Z.; Wang, J.; Li, Z.; Zeng, L.; Li, Y.; et al. IrW nanochannel support enabling ultrastable electrocatalytic oxygen evolution at 2 A cm^{-2} in acidic media. *Nature Communications* **2021**, *12* (1), 3540. DOI: 10.1038/s41467-021-23907-1.
(36) Wen, X.; Bai, L.; Li, M.; Guan, J. Ultrafine iridium oxide supported on carbon nanotubes for efficient catalysis of oxygen evolution and oxygen reduction reactions. *Materials Today Energy* **2018**, *10*, 153-160. DOI: https://doi.org/10.1016/j.mtener.2018.09.002.
(37) Fu, L.; Cai, P.; Cheng, G.; Luo, W. Colloidal synthesis of iridium-iron nanoparticles for electrocatalytic oxygen evolution. *Sustainable Energy & Fuels* **2017**, *1* (5), 1199-1203.
(38) Diaz-Morales, O.; Raaijman, S.; Kortlever, R.; Kooyman, P. J.; Wezendonk, T.; Gascon, J.; Fu, W. T.; Koper, M. T. M. Iridium-based double perovskites for efficient water oxidation in acid media. *Nature Communications* **2016**, *7* (1), 12363. DOI: 10.1038/ncomms12363.
(39) Xu, S.; Chen, S.; Tian, L.; Xia, Q.; Hu, W. Selective-leaching method to fabricate an Ir surface-enriched Ir-Ni oxide electrocatalyst for water oxidation. *Journal of Solid State Electrochemistry* **2016**, *20* (7), 1961-1970. DOI: 10.1007/s10008-016-3200-0.
(40) Massué, C.; Huang, X.; Tarasov, A.; Ranjan, C.; Cap, S.; Schlögl, R. Microwave-Assisted Synthesis of Stable and Highly Active Ir Oxohydroxides for Electrochemical Oxidation of Water. *ChemSusChem* **2017**, *10* (9), 1958-1968. DOI: https://doi.org/10.1002/cssc.201601864 (acccessed 2024/01/17).
(41) Tariq, M.; Zaman, W. Q.; Sun, W.; Zhou, Z.; Wu, Y.; Cao, L.-m.; Yang, J. Unraveling the Beneficial Electrochemistry of IrO_2/MoO_3 Hybrid as a Highly Stable and Efficient Oxygen Evolution Reaction Catalyst. *ACS Sustainable Chemistry & Engineering* **2018**, *6* (4), 4854-4862. DOI: 10.1021/acssuschemeng.7b04266.
(42) Zhang, T.; Liao, S.-A.; Dai, L.-X.; Yu, J.-W.; Zhu, W.; Zhang, Y.-W. Ir-Pd nanoalloys with enhanced surface-microstructure-sensitive catalytic activity for oxygen evolution reaction in acidic and alkaline media. *Science China materials* **2018**, *61*, 926-938.
(43) Zaman, W. Q.; Sun, W.; Tariq, M.; Zhou, Z.; Farooq, U.; Abbas, Z.; Cao, L.; Yang, J. Iridium substitution in nickel cobaltite renders high mass specific OER activity and durability in acidic media. *Applied Catalysis B: Environmental* **2019**, *244*, 295-302. DOI: https://doi.org/10.1016/j.apcatb.2018.10.041.
(44) Fu, L.; Yang, F.; Cheng, G.; Luo, W. Ultrathin Ir nanowires as high-performance electrocatalysts for efficient water splitting in acidic media. *Nanoscale* **2018**, *10* (4), 1892-1897.
(45) Lee, S. W.; Baik, C.; Kim, D.-H.; Pak, C. Control of Ir oxidation states to overcome the trade-off between activity and stability for the oxygen evolution reaction. *Journal of Power Sources* **2021**, *493*, 229689. DOI: https://doi.org/10.1016/j.jpowsour.2021.229689.
(46) Gou, W.; Zhang, M.; Zou, Y.; Zhou, X.; Qu, Y. Iridium-chromium oxide nanowires as highly performed OER catalysts in acidic media. *ChemCatChem* **2019**, *11* (24), 6008-6014.
(47) Zhang, J.; Wang, G.; Liao, Z.; Zhang, P.; Wang, F.; Zhuang, X.; Zschech, E.; Feng, X. Iridium nanoparticles anchored on 3D graphite foam as a bifunctional electrocatalyst for excellent overall water splitting in acidic solution. *Nano Energy* **2017**, *40*, 27-33. DOI: https://doi.org/10.1016/j.nanoen.2017.07.054.
(48) Shi, X.; Zhu, H.; Du, J.; Cao, L.; Wang, X.; Liang, H.-P. Directed assembly of ultrasmall nitrogen coordinated Ir nanoparticles for enhanced electrocatalysis. *Electrochimica Acta* **2021**, *370*, 137710. DOI: https://doi.org/10.1016/j.electacta.2020.137710.

(49) Fu, L.; Cheng, G.; Luo, W. Colloidal synthesis of monodisperse trimetallic IrNiFe nanoparticles as highly active bifunctional electrocatalysts for acidic overall water splitting. *Journal of Materials Chemistry A* **2017**, *5* (47), 24836-24841.
(50) Shan, J.; Guo, C.; Zhu, Y.; Chen, S.; Song, L.; Jaroniec, M.; Zheng, Y.; Qiao, S.-Z. Charge-redistribution-enhanced nanocrystalline Ru@IrO_x electrocatalysts for oxygen evolution in acidic media. *Chem* **2019**, *5* (2), 445-459.
(51) Jiang, B.; Kim, J.; Guo, Y.; Wu, K. C.; Alshehri, S. M.; Ahamad, T.; Alhokbany, N.; Henzie, J.; Yamachi, Y. Efficient oxygen evolution on mesoporous IrO_x nanosheets. *Catalysis Science and Technology* **2019**, *9* (14), 3697-3702.
(52) Tran, N. Q.; Le, T. A.; Kim, H.; Hong, Y.; Cho, Y.; Park, G. H.; Kim, H.; Kim, M.; Lee, J.; Yoon, W.-S.; et al. Low Iridium Content Confined inside a Co_3O_4 Hollow Sphere for Superior Acidic Water Oxidation. *ACS Sustainable Chemistry & Engineering* **2019**, *7* (19), 16640-16650. DOI: 10.1021/acssuschemeng.9b03982.
(53) Cao, L.; Luo, Q.; Chen, J.; Wang, L.; Lin, Y.; Wang, H.; Liu, X.; Shen, X.; Zhang, W.; Liu, W.; et al. Dynamic oxygen adsorption on single-atomic Ruthenium catalyst with high performance for acidic oxygen evolution reaction. *Nature Communications* **2019**, *10* (1), 4849. DOI: 10.1038/s41467-019-12886-z.
(54) Kresse, G.; Furthmuller, J. Efficient iterative schemes for ab initio total-energy calculations using a plane-wave basis set. *Physical Review B* **1996**, *54* (16), 11169-11186. DOI: DOI 10.1103/PhysRevB.54.11169.
(55) Kresse, G.; Furthmuller, J. Efficiency of ab-initio total energy calculations for metals and semiconductors using a plane-wave basis set. *Computational materials science* **1996**, *6* (1), 15-50. DOI: Doi 10.1016/0927-0256(96)00008-0.
(56) Larsen, A. H.; Mortensen, J. J.; Blomqvist, J.; Castelli, I. E.; Christensen, R.; Dulak, M.; Friis, J.; Groves, M. N.; Hammer, B.; Hargus, C.; et al. The atomic simulation environment-a Python library for working with atoms. *Journal of condensed matter physics* **2017**, *29* (27), 273002. DOI: ARTN 27300210.1088/1361-648X/aa680e.
(57) Hammer, B.; Hansen, L. B.; Norskov, J. K. Improved adsorption energetics within density-functional theory using revised Perdew-Burke-Ernzerhof functionals. *Physical Review B* **1999**, *59* (11), 7413-7421. DOI: DOI 10.1103/PhysRevB.59.7413.
(58) Zhang, H.; Soon, A.; Delley, B.; Stampfl, C. Stability, structure, and electronic properties of chemisorbed oxygen and thin surface oxides on Ir(111). *Physical Review B* **2008**, *78* (4), 045436. DOI: ARTN 04543610.1103/PhysRevB.78.045436.
(59) Yu, S.; Levell, Z.; Jiang, Z.; Zhao, X.; Liu, Y. What Is the Rate-Limiting Step of Oxygen Reduction Reaction on Fe–N–C Catalysts? *Journal of the American Chemical Society* **2023**, *145* (46), 25352-25356. DOI: 10.1021/jacs.3c09193.
(60) Zhao, X.; Liu, Y. Origin of Selective Production of Hydrogen Peroxide by Electrochemical Oxygen Reduction. *Journal of the American Chemical Society* **2021**, *143* (25), 9423-9428. DOI: 10.1021/jacs.1c02186.
(61) Man, I. C.; Su, H.-Y.; Calle-Vallejo, F.; Hansen, H. A.; Martínez, J. I.; Inoglu, N. G.; Kitchin, J.; Jaramillo, T. F.; Nørskov, J. K.; Rossmeisl, J. Universality in Oxygen Evolution Electrocatalysis on Oxide Surfaces. *ChemCatChem* **2011**, *3* (7), 1159-1165. DOI: https://doi.org/10.1002/cctc.201000397 (acccessed 2024/04/24).
(62) Seitz, L. C.; Dickens, C. F.; Nishio, K.; Hikita, Y.; Montoya, J.; Doyle, A.; Kirk, C.; Vojvodic, A.; Hwang, H. Y.; Norskov, J. K.; et al. A highly active and stable $IrO_x/SrIrO_3$ catalyst for the oxygen evolution reaction. *Science* **2016**, *353* (6303), 1011-1014. DOI: 10.1126/science.aaf5050.
(63) Liu, S.; White, M. G.; Liu, P. Mechanism of oxygen reduction reaction on Pt(111) in alkaline solution: Importance of chemisorbed water on surface. *Journal of Physical Chemistry C* **2016**, *120* (28), 15288–15298.
(64) Ma, Z.; Zhang, Y.; Liu, S.; Xu, W.; Wu, L.; Hsieh, Y.-C.; Liu, P.; Zhu, Y.; Sasaki, K.; Renner, J. N.; et al. Reaction mechanism for oxygen evolution on RuO_2, IrO_2, and RuO_2@IrO_2 core-shell nanocatalysts. *Journal of Electroanalytical Chemistry* **2018**, *819*, 296-305. DOI: https://doi.org/10.1016/j.jelechem.2017.10.062.
(65) Ayers, K. E.; Renner, J. N.; Danilovic, N.; Wang, J. X.; Zhang, Y.; Maric, R.; Yu, H. Pathways to ultra-low platinum group metal catalyst loading in proton exchange membrane electrolyzers. *Catalysis Today* **2016**, *262*, 121-132. DOI: https://doi.org/10.1016/j.cattod.2015.10.019.
(66) Lee, J. H.; Kattel, S.; Jiang, Z.; Xie, Z.; Yao, S.; Tackett, B. M.; Xu, W.; Marinkovic, N. S.; Chen, J. G. Tuning the activity and selectivity of electroreduction of CO_2 to synthesis gas using bimetallic catalysts. *Nature Communications* **2019**, *10* (1), 3724. DOI: 10.1038/s41467-019-11352-0.

Insert Table of Contents artwork here